Covalent Grafting of Ruthenium Complexes on Iron Oxide Nanoparticles: Hybrid Materials for Photocatalytic Water Oxidation

Quyen Nguyen Thi, Elodie Rousset, van T. H. Nguyen, Vincent Collière, Pierre Lecante, Wantana Klysubun, Karine Philippot, Jérôme Esvan, Marc Respaud, Gilles Lemercier, et al.

Covalent Grafting of Ruthenium Complexes on Iron Oxide Nanoparticles: Hybrid Materials for Photocatalytic Water Oxidation

Quyen T. Nguyen, Elodie Rousset, Van T. H. Nguyen, Vincent Colliere, Pierre Lecante, Wantana Klysubun, Karine Philippot, Jérôme Esvan, Marc Respaud, Gilles Lemercier,* Phong D. Tran,* and Catherine Amiens*

ABSTRACT: The present environmental crisis prompts the search for renewable energy sources such as solar driven production of hydrogen from water. Herein, we report an efficient hybrid photocatalyst for water oxidation, consisting of a ruthenium polypyridyl complex covalently grafted on core/shell Fe@FeO_x nanoparticles *via* a phosphonic acid group. The photoelectrochemical measurements were performed under 1 sun illumination in 1 M KOH. The photocurrent density of this hybrid photoanode reached 20 $\mu A/cm^2$ (applied potential of +1.0 V *vs* reversible hydrogen electrode), corresponding to a turnover frequency of 0.02 s^{-1}. This performance represents a 9 fold enhancement of that achieved with a mixture of Fe@FeO_x nanoparticles and a linker free ruthenium polypyridyl photosensitizer. This increase in performance could be attributed to a more efficient electron transfer between the ruthenium photosensitizer and the Fe@FeO_x catalyst as a consequence of the covalent link between these two species through the phosphonate pendant group.

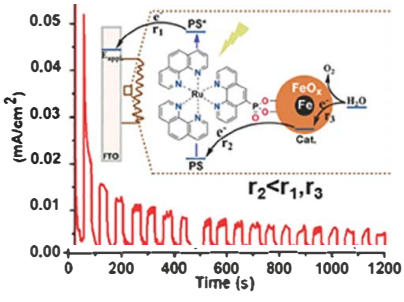

KEYWORDS: *covalent grafting, hybrid photoanode, iron oxide nanoparticles, ruthenium based photosensitizer, water oxidation catalysis*

1. INTRODUCTION

The 21st century has seen a boom in the development of renewable energy sources, as the world attempts to transition from the serious environmental and health issues associated with the use of non renewable sources such as coal or oil. In this context, hydrogen gas evolved from solar water splitting has attracted tremendous interest as a green fuel.[1] Solar driven water splitting is a thermodynamically uphill process comprising two sluggish half reactions: the oxygen evolution reaction (OER) and the hydrogen evolution reaction (HER). It can be accomplished in a photoelectrochemical cell comprising a photoanode where the OER takes place with solar energy input, and a photocathode (or a simple cathode) where the HER occurs. As the OER is more challenging to achieve, a large research effort focuses nowadays on the development of appropriate photoanodes. In general, a photoanode is constituted of a *photosensitizer* (PS) for photon harvesting and a *catalyst* for accelerating the OER. N type semiconductors such as TiO_2,[2] $BiVO_4$,[3] and α Fe_2O_3[4] or molecular dyes such as ruthenium tris bipyridine complexes,[5,6] perylene,[7,8] polyheptazine,[9,10] metal free porphyrins,[11] and π conjugated naphthalene benzimidazole polymers[12] have been assayed as PSs in this context. Regarding the OER catalyst, oxides of transition metals such as IrO_2,[13,14] CoO_x,[15,16] Co–Pi,[17−19] or FeOOH[20−23] have been investigated, as well as some molecular complexes.[24,25]

To build the photoanode, a dyad comprising a molecular complex catalyst linked to a molecular PS can be deposited on a transparent electrode.[26,27] The molecular catalyst can also be combined with an N type semi conducting material as a PS. This can be done either by simple physical adsorption or by covalent grafting. This second strategy may lead to photo anodes with improved performance[28] if it can provide (i) an improved electron/hole transfer between the two components and, beyond, an enhanced overall photocatalytic activity and (ii) a more robust system preventing the leaching out of the catalyst.

When a metal oxide catalyst is employed, it can also be combined with an N type semi conducting material acting as a PS. In this case, the two materials are generally interfaced without any specific linker to create a solid−solid junction.[16,19,29−31] Altematively, a hybrid photoanode can be engineered by covalently grafting a molecular PS onto the surface of the metal oxide catalyst. Similarly, when a molecular catalyst is grafted on a solid PS, such covalent grafting between the molecular PS and solid catalyst is believed to offer (i) an efficient electron/hole transfer between the two components and (ii) a more robust system preventing the leaching out of

https://doi.org/10.1021/acsami.1c15051

the PS. To the best of our knowledge, the first example of such a photoanode for solar water splitting was reported by Mallouk and co workers in 2009, wherein a ruthenium tris bipyridine complex, acting as a PS, was covalently grafted through a malonate linker on IrO_2 nanoparticles (NPs), used here as a catalyst.[32] Since then, only a few other systems were published.[7,33] Recently, our group also investigated this approach and reported the covalent grafting of a Ru complex PS onto Co_3O_4 NPs, using pendant phosphonate linkers and its positive impact on the photoanode efficiency.[34] We then expanded our work toward more environment friendly catalysts, such as iron based systems, considering that iron oxides[35,36] and iron oxohydroxides[20−23] have been reported to be active and stable electrocatalysts for the OER, but that none of these materials have been used so far to build a hybrid photoanode by combination with a molecular PS.

Ruthenium trispolypyridyl complexes are archetypal molec ular PSs[37−39] as they present large extinction coefficients over a broad range of the visible spectrum, a long lived excited state, and high luminescent quantum yields. This allows an efficient energy/electron transfer to the catalyst. Their scaffold is also highly tunable, allowing the fine tuning of the optical properties and redox potentials. In comparison with the archetypal $[Ru(bpy)_3]^{2+}$ that is mainly used in the develop ment of photo electrocatalytic systems, the phenanthroline based analogues present a wide interest due to their more rigid and conjugated ligands.[40,41] This type of complex is also air stable and displays a high thermal stability allied to a remarkable chemical inertness.[42,43] In our study, a pendant phosphonate group was introduced on the fifth position of one of the 1,10 phenanthroline ligands, as such functional groups are reported to afford a covalent grafting onto iron oxide surfaces.[44−47] This position is usually substituted as it offers efficient charge transfers in photophysical applications, and it is the less sterically hindered in the resulting complex, potentially allowing an easier grafting on the NPs.

We report herein an unprecedented robust hybrid photo catalyst for OER where ruthenium trisphenanthroline com plexes (as PSs) are grafted on core/shell iron@iron oxide NPs (**Fe@FeO$_x$ NPs**) used as a catalyst (Figure 1). This hybrid photocatalyst was deposited onto a fluoride doped tin oxide (FTO) electrode to generate a novel hybrid photoanode. Its photocatalytic activity was assayed to evaluate the interest of the covalent coupling between the PS and catalyst.

2. RESULTS AND DISCUSSION

2.1. Synthesis and Characterization of the OER Catalyst. In previous studies, we demonstrated that the grafting of a phosphonic group was more efficient on NPs showing a substantial iron oxide layer at their surface.[48] Thus, in this work, we prepared **Fe@FeO$_x$** core/shell NPs presenting a crystalline iron oxide shell. A two step procedure was followed (Scheme 1). First, body centered cubic (bcc) iron NPs (Fe NPs) were prepared following the procedure reported by Gharbi *et al.*[48] Then, based on the work of Peng *et al.*,[49] the controlled oxidation of these native NPs was performed to generate an iron oxide shell. Analysis by transmission electron microscopy (TEM) showed that the obtained NPs displayed a mean size of 11.5 ± 2.3 nm and a "flower like" morphology (Supporting Information, Figure S1). Their study under high resolution conditions confirmed that this discontinuous shell of lighter contrast (Figure 2a) consisted in well defined iron oxide

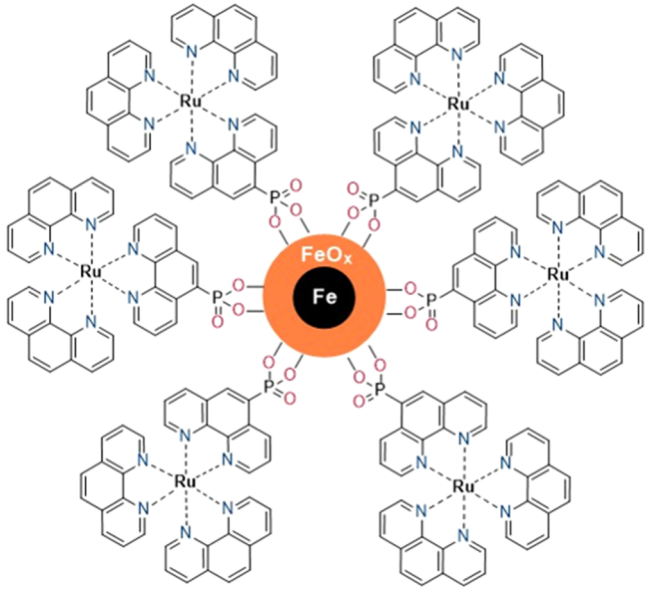

Figure 1. Schematic view of the hybrid nanomaterial where Ru(II) tris(1,10 phenanthroline) complexes are grafted onto the **Fe@FeO$_x$ NPs** *via* a phosphonate group.

crystalline grains (Figure 2b and Supporting Information, Figure S1c,d).

The crystallinity of the oxide shell was further evidenced, on a more statistical basis, through wide angle X ray scattering (WAXS) measurements. The diagram obtained for the **Fe@ FeO$_x$ NPs** is presented in Figure 3, together with bcc Fe (α Fe), γ Fe_2O_3 (maghemite), and NH_4Cl reference diagrams. Diffraction peaks at 10, 15, and 26° were assigned to NH_4Cl, a product issued from a side reaction between HDA·HCl and hexamethyldisilazane in the first step of the synthesis, as already reported by our group.[50] We also observed peaks assignable to γ Fe_2O_3 and to bcc Fe, clearly demonstrating the formation of a crystalline oxide shell around the iron core.

The persistence of the iron core was also probed by extended X ray absorption fine structure (EXAFS) at the Fe K absorption edge. Contrarily to WAXS, which places a strong emphasis on large crystalline domains, EXAFS is strictly limited to short range order. On the other hand, this limitation makes it much more sensitive for the analysis of small domains, and contributions not involving Fe atoms would be rejected in principle. A pure Fe foil was measured under the same conditions as **Fe@FeO$_x$ NPs** and additional reference data from the pure γ Fe_2O_3 were imported from the Farrel Lytle database. Comparing the χ function of the **Fe@FeO$_x$ NPs** with those of the two references (Supporting Information, Figure S2), the pattern of γ Fe_2O_3 was clearly observed with, however, some discrepancies (in the 8.2−9.5 $Å^{-1}$ range). Interestingly, these discrepancies could be clearly attributed to metallic Fe features. A model including the short Fe−O bonding distance and the longer Fe−Fe distance with an O bridge typical of an iron oxide, as well as the metallic bonding Fe−Fe distance, allowed a good fit of the experimental data, especially in the 6−10 $Å^{-1}$ range (Table S1, Figure S3). Good agreement was also observed for the Fourier transform (Figures 4 and S4). A model considering more shells could likely provide even better agreement but without providing more insights on this composite sample which likely includes Fe(III) oxide at different degrees of crystallization. For the same reason,

Scheme 1. Synthetic Pathway of the Fe@FeO$_x$ Core/Shell NPs

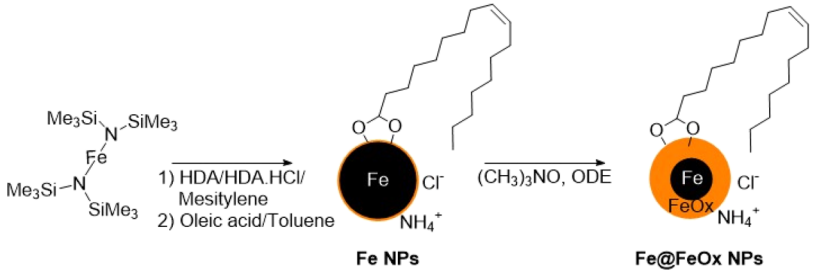

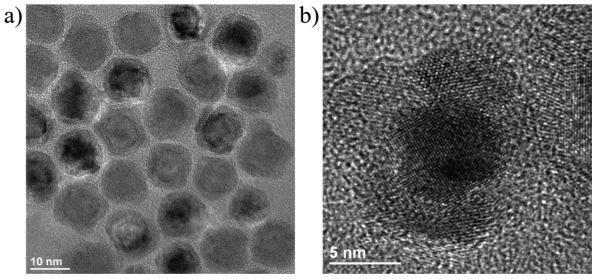

Figure 2. Typical HR TEM images of the **Fe@FeO$_x$ NPs** with different scale bars: (a) 10 and (b) 5 nm.

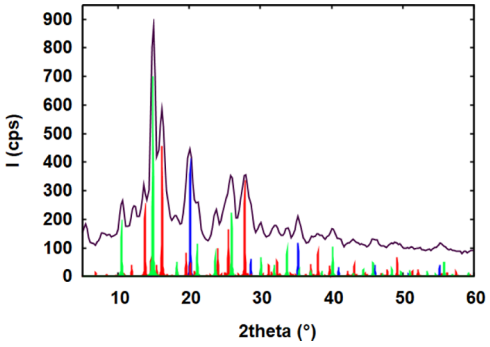

Figure 3. WAXS diagram of the **Fe@FeO$_x$ NPs** (black solid line) in comparison with those of bcc Fe (PDF 01 071 4648, in blue), γ Fe_2O_3 (PDF 01 089 5894, in red), and NH_4Cl (PDF 96 901 0007, in green) references.

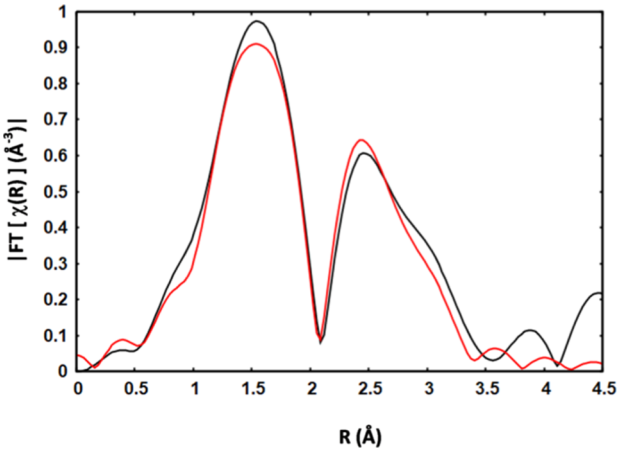

Figure 4. Magnitude of the Fourier transform of function $\chi(R)$ from the **Fe@FeO$_x$ NPs** (black line) and the best fit achieved (red line).

quantitative evaluation of the Fe/Fe oxide ratio was not attempted even if a mixed organization was demonstrated.

From the Fe 2p spectrum obtained by X ray photoelectron spectroscopy (XPS) (Supporting Information, Figure S5), only binding energies corresponding to Fe(0) (706.7 eV) and Fe(III) in an iron oxide environment (710.3 eV) were observed. This confirmed the presence of a residual Fe core and indicated that the oxide shell was most likely α or γ Fe_2O_3, even if the presence of FeOOH species on the top surface could not be excluded.

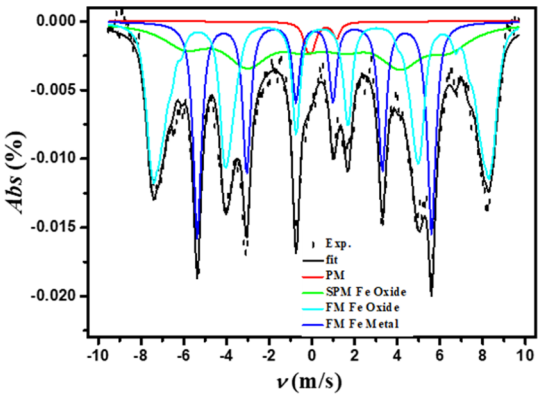

Figure 5. Mössbauer spectrum of the **Fe@FeO$_x$ NPs** recorded at 80 K (experimental data in black markers), and the best fit obtained (solid line) from a combination of iron and iron oxide contributions (see legend in the figure).

A quantitative evaluation of the Fe/FeO$_x$ ratio in the NPs and identification of the oxide formed were obtained from the Mössbauer spectrum (Figure 5, Table S2) recorded at 80 K. At this temperature, and given the size of the NPs, relaxation phenomena on the time scale of Mössbauer spectroscopy (10^{-11} to 10^{-9} s) were initially expected to be negligible. Given the morphology of the NPs, the defined lines observed in the spectrum could be attributed to the contributions of ferromagnetic iron (FM Fe, 28.9 ± 0.5%) and iron oxide phases (FM Fe oxide, 42.9 ± 0.5%). However, to precisely adjust the experimental curve, two other contributions had to be introduced: the first one corresponding to iron oxide in superparamagnetic regime (SPM Fe oxide, 26.2 ± 0.5%) and the second one corresponding to a trace of paramagnetic iron (PM Fe, 2.0 ± 0.2%). Table S2 and Figure S6 display the hyperfine fields, quadrupolar splitting, and the corresponding isomer shifts used to fit the spectrum. The parameters used to fit the iron oxide contributions are in good agreement with those expected for γ Fe_2O_3 at the nanoscale.[51] The two contributions observed (one FM and the other SPM) could reflect the heterogeneity of the iron oxide shell thickness and polycrystallinity. The Fe(0)/Fe(III) atomic ratio extracted from fitting the Mössbauer spectrum indicated an average shell

thickness of 2.6 nm (Supporting Information, Section S1.5). Thus, the **Fe@FeO$_x$ NPs** can be best described as core/shell Fe@γ Fe_2O_3 NPs with a mean size of 11.5 ± 2.3 nm and an average shell thickness of 2.6 nm. We note that having the γ Fe_2O_3 phase on the NP shell is highly desirable as this phase is more catalytically active for the water oxidation reaction than the α Fe_2O_3 phase.[36] We then treated these core/shell Fe@γ Fe_2O_3 NPs with the **[Ru−PO(OH)$_2$]Cl$_2$** complex in order to create the hybrid photocatalyst.

2.2. Synthesis and Characterization of the Hybrid Photocatalyst. The synthesis of the 5 phosphonic 1,10 phenanthroline ligand and Ru complex (hereafter referred to as **[Ru−PO(OH)$_2$]Cl$_2$**) were adapted from those reported for the synthesis of 2,2′ bipyridine[52] and of bis heteroleptic ruthenium(II) complexes[53,54] (see Scheme S1, Figures S8−S11 in the Section S2 of Supporting Information for details). The resulting complex **[Ru−PO(OH)$_2$]Cl$_2$** absorbs in the visible domain and is emissive through its ^{3}MLCT excited state (Supporting Information, Figures S12−S14), showing similar photophysical properties to the $[Ru(phen)_3]^{2+}$ reference complex.

Scheme 2. Synthetic Pathways for the Hybrid Photocatalysts Prepared in a Biphasic Medium (*b* Fe@FeO$_x$@Ru NPs) or in a Monophasic Medium (*m* Fe@FeO$_x$@Ru NPs)

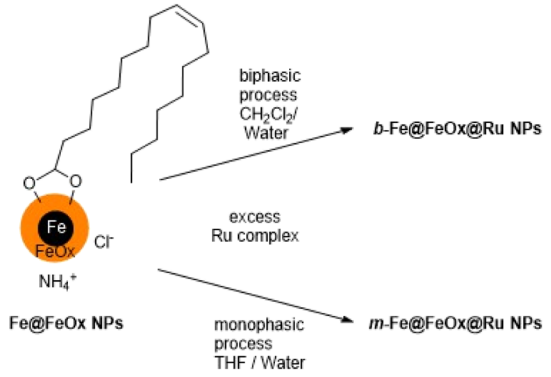

Two synthetic pathways were developed to graft the **[Ru−PO(OH)$_2$]Cl$_2$** complex on the **Fe@FeO$_x$ NPs** (Scheme 2). At first, a biphasic method previously used to graft 3 amino phosphonic acid on similar NPs was followed (Figure S15).[48] However, it afforded only a poor grafting density of the Ru complex on the iron oxide surface (9 Ru complexes per NP, sample hereafter called **b Fe@FeO$_x$@Ru NPs**, b standing for biphasic) (Supporting Information, Section S3.3, Figure S16).

A monophasic method was then implemented, in which **Fe@FeO$_x$ NPs** and **[Ru−PO(OH)$_2$]Cl$_2$** were added to a homogeneous THF−water phase (Supporting Information Section S3.2, Figure S17). The magnetic component was recovered from the resulting suspension by magnetic separation. The resulting samples, hereafter referred to as *m* Fe@FeO$_x$**@Ru NPs** (m standing for monophasic), were washed 5 times with Milli Q water, 1 time with ethanol, and 1 time with diethyl ether to remove the non grafted ruthenium complex. Analysis of high resolution high angle annular dark field scanning TEM (HR HAADF STEM) images of the *m* Fe@FeO$_x$**@Ru NPs** showed that the core/shell morphology of the parent NPs was preserved, but suggested a thicker iron oxide shell (Figure 6). Accordingly, the crystalline iron oxide component was now the dominant feature of the WAXS

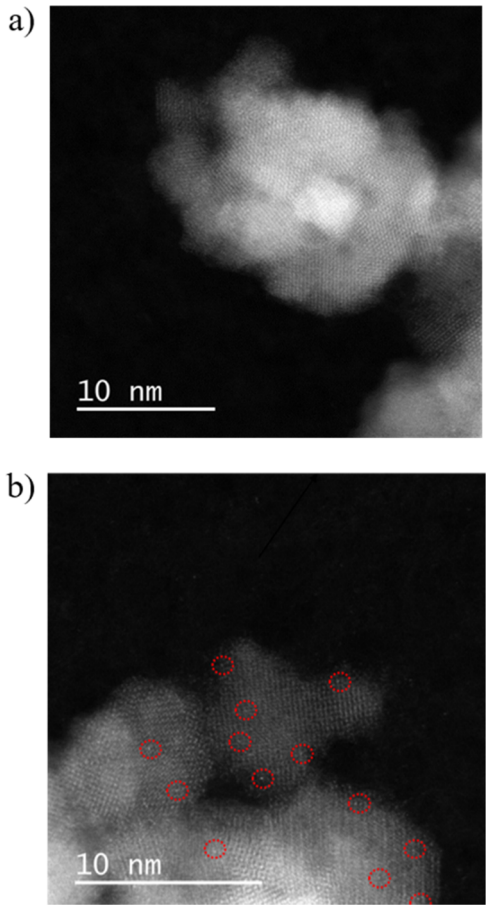

Figure 6. HR HAADF STEM analysis of the *m* Fe@FeO$_x$**@Ru NPs**: (a) typical NP image and (b) atomic resolution micrograph showing the presence of dispersed Ru atoms (highlighted by red cycles).

diagram (Figure 7).[55] The width of the peak at 2θ = 20° and the presence of a peak at 2θ = 35° suggested a very small contribution of metallic Fe even though it could not be confirmed, nor disproved. The growth of the oxide layer at the expense of the iron core was further confirmed by XPS as in the Fe 2p region only one peak at 710.2 eV, attributed to Fe^{3+}, was observed (Supporting Information, Figure S19).

The grafting of the Ru complex on the NPs was first indicated by the presence of the dispersed bright dots in the HR HAADF STEM images of the sample (Figure 6b). As the atomic number *Z* of a Ru atom is higher than that of an Fe

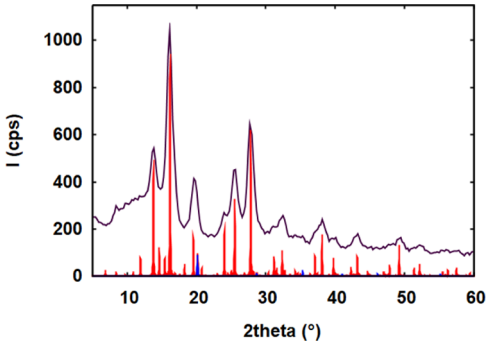

Figure 7. WAXS diagram of the *m* Fe@FeO$_x$**@Ru NP** sample (black solid line) in comparison with γ Fe_2O_3 (PDF 01 089 5894, in red) and bcc Fe (PDF 01071 4648, in blue) references.

atom, these bright dots were tentatively attributed to Ru atoms from the grafted Ru complexes. The integrity of the Ru complexes was evidenced by XPS. Spectra collected in the Ru 3d and C 1s energy ranges on the *m* Fe@FeO$_x$**@Ru NPs**, **Fe@FeO$_x$ NPs**, and **[Ru−PO(OH)$_2$]Cl$_2$** complex are shown in Figure 8. The free Ru complex showed a Ru 3d$_{5/2}$ peak at

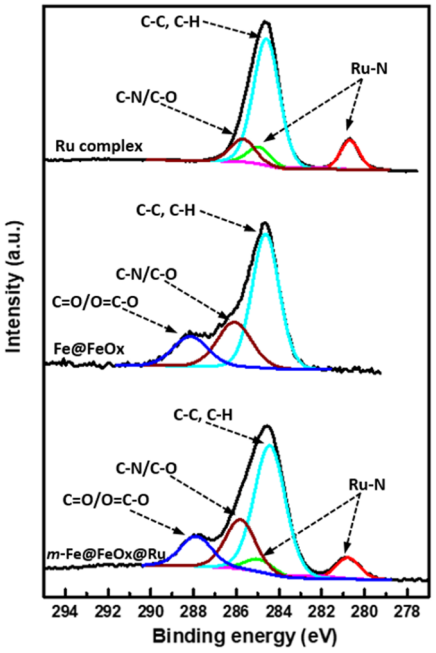

Figure 8. XPS spectra of the free ruthenium complex [**Ru−PO(OH)$_2$]Cl$_2$** (top), **Fe@FeO$_x$ NPs** (middle), and *m* Fe@FeO$_x$**@Ru NPs** (bottom) in the C 1s−Ru 3d region (red and green curves: Ru−N 3d$_{5/2}$ and 3d$_{3/2}$ signals, respectively; cyan curve: C−C/C−H signal; brown curve: C−N/C−O signal; and blue curve: C═O/O═C−O signal).

binding energy of 280.7 eV, being characteristic of a Ru−N environment.[56] The Ru 3d$_{3/2}$ peak associated was observed at 285 eV (Supporting Information, Table S3). Two similar peaks were observed for the *m* Fe@FeO$_x$**@Ru NPs** but not for the **Fe@FeO$_x$ NPs**. In the *m* Fe@FeO$_x$**@Ru NPs** spectrum, a N 1s peak attributed to the N−Ru bond was observed at 399.8 eV (Supporting Information, Figure S20). Interestingly, we did not observe any contribution from N in an ammonium environment (expected at 401.9 eV[57]) confirming again the elimination of NH_4Cl during the grafting process, as observed in the WAXS measurements (Supporting Information, Figure S18). Furthermore, in the *m* Fe@FeO$_x$**@Ru NPs** spectrum, the C 1s peak at 284.7 eV could be attributed to C−C/C−H bonds from the phenanthroline ligand and/or from the oleic acid used during the NP synthesis and retained on their surface, whereas the peak at a higher binding energy (285.8 eV) could be attributed to the C−N bond of the phenanthro line ligand and/or the C−O bond of the oleic acid. The persistence of some oleic acid at the surface of the NPs was further confirmed by the peak at 288 eV, assigned to C═O/O−C═O bonds, which was observed in the spectra of both the **Fe@FeO$_x$ NPs** and *m* Fe@FeO$_x$**@Ru NPs** (Figure 8 and Supporting Information, Table S3), but not in the spectrum of the Ru complex. The persistence of oleic acid evidences that the exchange of the carboxylic acid coating of the NPs by phosphonates is difficult at room temperature, even when an excess of phosphonate is introduced.[45]

The Ru complex content in the *m* **Fe@FeO$_x$@Ru NPs** was quantitatively determined by inductively coupled plasma optical emission spectroscopy (ICP OES) at *ca.* 56 Ru complexes per NP against *ca.* 9 Ru complexes per NP in the *b* Fe@FeO$_x$**@Ru NPs** (*see Supporting Information Section S3.3 for calculation details*).

All these data clearly provide evidence of the presence of the Ru complex on the surface of the *m* Fe@FeO$_x$**@Ru NPs** although much less Ru complex was grafted *via* the biphasic method than *via* the monophasic one. The higher grafting density obtained by the monophasic method may arise from more efficient interactions between the ruthenium complexes and the NPs due to the miscibility of the solvents, while in the biphasic method such interactions can happen only at the water/dichloromethane interface.

2.3. Electrocatalytic Activity of Fe@FeO$_x$ NPs in Water Oxidation. In the prepared (*m*/*b*) Fe@FeO$_x$**@Ru** hybrid systems, the role of the molecular complex is to harvest solar energy, whereas the **Fe@FeO$_x$** core aims to accelerate the water oxidation reaction. Thus, before investigating the photocatalytic activity of these hybrid systems, the electro catalytic activity of the **Fe@FeO$_x$ NPs** was evaluated. To this end, a catalyst ink made of **Fe@FeO$_x$ NPs** in a EtOH/water solvent mixture together with 1 μL Nafion 5% (wt %) as a linker was drop casted on a FTO electrode at a mass loading density of 1.8×10^{-4} g/cm^2 (Supporting Information, Figure S21). The resulting catalyst electrode was then assayed in a pH 7 phosphate buffer (KPi 0.1 M) and a pH 13 alkaline electrolyte (NaOH 0.1 M). At pH 13, it operated with an onset potential of ∼1.75 V *versus* reversible hydrogen electrode (RHE) and a Tafel slope value of 142 mV/decade could be deduced from the polarization curves (Figure 9, black trace). At pH 7, it showed a much higher onset potential of ∼1.95 V as well as a higher Tafel slope value: 207 mV/decade (Figure 9, red trace). This assay demonstrated that the **Fe@FeO$_x$ NPs** is an active catalyst for the OER, and that it is significantly more active in an alkaline solution.

2.4. Photoelectrochemical Water Oxidation Catalysis with Fe@FeO$_x$@Ru Hybrid Electrodes. We investigated the photocatalytic activity of the **Fe@FeO$_x$@Ru NPs** hybrid nanomaterials to understand to what extent a covalent linkage between the molecular PS and the nanocatalyst can benefit its overall operation. To this end, an ink was prepared from the **Fe@FeO$_x$@Ru NPs** samples and deposited onto a FTO electrode as described above for the **Fe@FeO$_x$ NPs**. The light source was provided by a Xe arc lamp equipped with a UV filter. We employed the back illumination mode in which the incident light went through the transparent FTO electrode to the catalyst. The incident light intensity reaching the FTO electrode was set to 100 mW/cm^2.

Figure 10a shows a simplified overview of the electron transfers involved during the operation of the hybrid photocatalyst. In this model, the overall oxygen production rate is determined by the slowest step of the elemental reactions 1, 2, and 3, in which: (i) r_1 represents the rate of the oxidation of the excited photosensitizer (PS*) by an oxidative potential applied to the FTO electrode. Thus, r_1 is expected to increase when an increasing oxidative potential is applied; (ii) r_2 represents the electron transfer rate from the catalyst to the oxidized photosensitizer (PS^+) (*i.e.*, the hole transfer rate from PS^+ to the catalyst), and (iii) r_3 represents the O_2 evolution

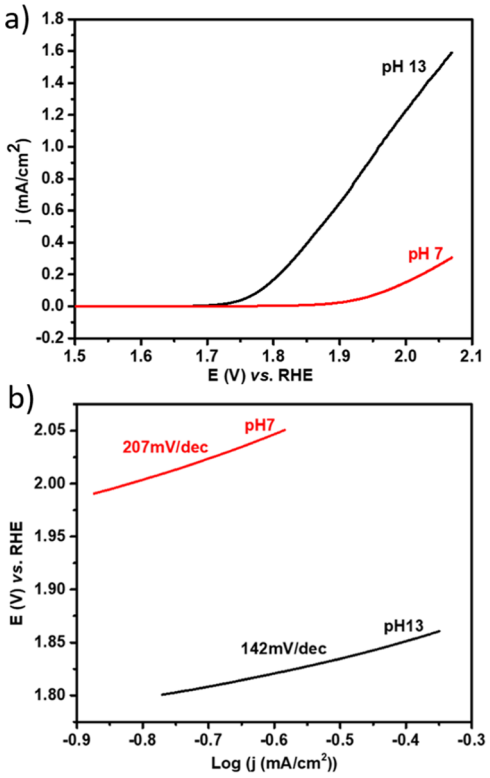

Figure 9. (a) Polarization curves of an **Fe@FeO$_x$ NP** electrode recorded in pH 7 (red line) and pH 13 (black line) electrolyte solutions. Potential scan rate: 5 mV/s. (b) Tafel plots of the **Fe@FeO$_x$ NP** electrode at pH 7 (red line) and pH 13 (black line).

rate on the surface of the water oxidation catalyst, that is, on the surface of the **Fe@FeO$_x$** component of the hybrid nanomaterial.

Herein, the photocatalytic activity of the *m* Fe@FeO$_x$**@Ru NP** electrode for the water oxidation reaction was assayed at pH 13, where r_3 is assumed to be optimal. In these conditions, an **Fe@FeO$_x$** control electrode was not photocatalytically active, showing negligible photogenerated current under 1 sun illumination (Figure 10b, blue and pink traces). A negligible current density was also recorded for the *m* Fe@FeO$_x$**@Ru NP** electrode under dark condition at applied potentials up to 1.5 V *versus* RHE (Figure 10b, black trace). Under light illumination, the onset potential for generating a measurable photocurrent was found to be 0.75 V *versus* RHE. An almost constant photocurrent density was observed when increasing the applied potential up to 1.1 V *versus* RHE. This means that the overall rate of water oxidation remained unchanged in this potential window, even if r_1 should increase when increasing the applied oxidative potential. Therefore, the charge transfer between the Ru PS and the **Fe@FeO$_x$** nanocatalyst, namely r_2, limited the whole operation in this potential range.

In order to emphasize the benefit of engineering a covalent grafting between the PS and the catalyst, we also recorded the photocatalytic activity of a simple mixture of **Fe@FeO$_x$ NPs** and ruthenium tris phenanthroline chloride, $[Ru(phen)_3]Cl_2$, in the same Ru per NP ratio (*i.e.,* 56) as in the *m* Fe@FeO$_x$**@Ru NP** sample, hereafter labeled **Fe@FeO$_x$//Ru**. $[Ru(phen)_3]Cl_2$ was chosen as a reference PS given its comparable photophysical properties to those of **$[Ru-PO(OH)_2]Cl_2$** (see Supporting Information, Figure S13) and was expected to adsorb only physically onto the **Fe@FeO$_x$ NPs** given the absence of pendant grafting groups. A control electrode was also fabricated by loading only **Fe@FeO$_x$ NPs** at an identical mass loading density without adding any Ru complex. Figure 11a shows the *I*–*t* curves recorded at 1.0 V *versus* RHE under chopped light mode using electrodes made of *m* Fe@FeO$_x$**@Ru NPs** (red trace), **Fe@FeO$_x$//Ru** (blue trace), and **Fe@FeO$_x$ NPs** (black trace). The **Fe@FeO$_x$ NP** photoanode generated a negligible photocurrent density of *ca.* 0.5 μA/cm^2. **Fe@FeO$_x$//Ru** (simple mixture) showed a higher photocurrent density (2.3 μA/cm^2) demonstrating the improvement in light harvesting brought by the Ru complex. Interestingly, a significantly higher photocurrent density of *ca.* 20 μA/cm^2 was achieved for the *m* Fe@FeO$_x$**@Ru NP** electrode (where the Ru complex is covalently grafted on the **Fe@FeO$_x$** nanocatalyst). This value corresponds to *ca.* 9 fold and 40 fold higher activities than those obtained with the **Fe@FeO$_x$//Ru** and **Fe@FeO$_x$** electrodes, respectively. This result clearly demonstrates, as suggested in the literature,[34,58] the usefulness of a covalent grafting between the Ru PS and the **Fe@FeO$_x$** catalyst to promote the charge transfer and therefore increase the overall photocatalytic activity.

The robustness of our hybrid system was evaluated by repeating the on–off light illumination cycle. The *m* Fe@FeO$_x$**@Ru NP** photoanode was found to still produce ~50% of the initial photocurrent density (determined in the first on–off

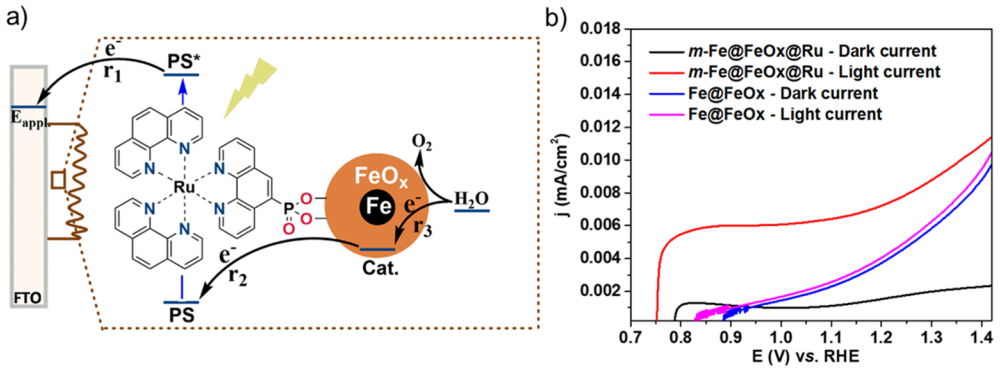

Figure 10. (a) Simplified scheme for the photocatalytic water oxidation where PS and PS* stand for the photosensitizer in its ground and excited states, respectively, and cat stands for the catalyst (here the **Fe@FeO$_x$ NPs**). (b) *I*–*V* curves recorded on the *m* Fe@FeO$_x$**@Ru NP** (dark: black trace; illumination: red trace) and the **Fe@FeO$_x$ NP** (dark: blue trace; illumination: pink trace) photoanodes immersed in a pH 13 (NaOH 0.1 M) electrolyte. Potential scan rate: 10 mV/s, 1 sun illumination.

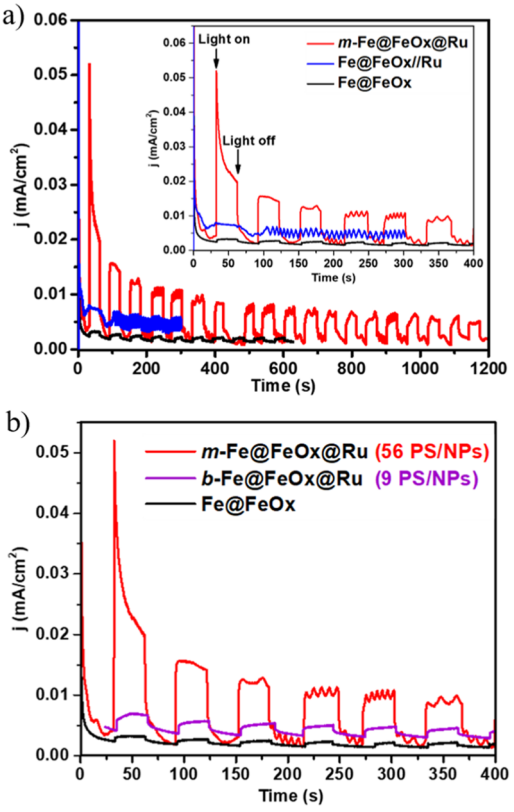

Figure 11. (a) *I*–*t* curves recorded on *m* Fe@FeO$_x$**@Ru NP** (red trace), **Fe@FeO$_x$//Ru** (blue trace), and **Fe@FeO$_x$ NP** (black trace) photoanodes; (b) *I*–*t* curves recorded on *m* Fe@FeO$_x$**@Ru NP** (red trace), *b* Fe@FeO$_x$**@Ru NP** (purple trace), and **Fe@FeO$_x$** NP (black trace) photoanodes. Applied potential: 1.0 V *vs* RHE. Electrolyte: pH 13 NaOH solution. Light incident power intensity: 100 mW/cm^2.

cycle) after 20 min assay, whereas the non bonded **Fe@FeO$_x$//Ru** counterpart did not generate any noticeable photocurrent from the second on–off cycle onward. Thus, the covalent grafting significantly improves the stability of the *m* Fe@FeO$_x$**@Ru NP** hybrid system. The degradation of the non bonded **Fe@FeO$_x$//Ru** system can be attributed to a fast detachment of $[Ru(phen)_3]Cl_2$ from the electrode surface because of the lack of covalent bonding and the high solubility of this complex in water. It can be also attributed to a rapid decomposition of $[Ru(phen)_3]Cl_2$ due to the lack of an efficient electron communication with the **Fe@FeO$_x$ NP**.

As described above, the *b* Fe@FeO$_x$**@Ru NPs** had a much lower Ru complex grafting density than the *m* Fe@FeO$_x$**@Ru NPs**, that was, 9 Ru complexes *versus* 56 Ru complexes per NP. At identical mass loading density, the *b* Fe@FeO$_x$**@Ru NP** photoanode showed a 7 fold lower photocurrent density than the *m* Fe@FeO$_x$**@Ru NP** photoanode did, that was ~3 *versus* ~20 μA/cm^2 (Figure 11b, purple and red traces). However, comparable photocatalytic performances were deduced for these two photoanodes when normalizing the catalytic activity per number of PS, that was, per number of grafted Ru complex (see Supporting Information, *Section S4 for details on normalization*), thus confirming that the rate limiting step involved the Ru complex. Turnover frequencies per Ru complex (TOF_{Ru}) of 0.015 and 0.02 s^{-1} were calculated for the photoanodes prepared with the *b* Fe@FeO$_x$**@Ru NPs** and *m* Fe@FeO$_x$**@Ru NPs**, respectively. The similarity of these values further confirmed that the charge transfer between the Ru PS and the **Fe@FeO$_x$** nanocatalyst was the main limiting factor. A higher density of the Ru PS would thus increase the overall performance of the system.

Looking back at the first on–off light illumination cycle recorded with the *m* Fe@FeO$_x$**@Ru NPs**, a high transient photocurrent ($\Delta J_{transient}$) of 33 μA/cm^2 (Supporting Information, Figure S22) was observed. This suggested an important charge recombination within the system.[59,60] More studies are required to understand this phenomenon. For now, we tentatively attribute this recombination to the quenching of the (luminescent) ^{3}MLCT excited state of the Ru PS[61] by the oxygen molecules which are generated locally on the surface of the **Fe@FeO$_x$ NPs**. Such a quenching has been indeed demonstrated in solution, as mentioned earlier in this study (Supporting Information, Figure S14). If so, quickly removing oxygen from the catalyst surface would reduce the charge recombination and thus represents a good strategy to increase the performance of the hybrid photocatalyst.

3. CONCLUSIONS

This study reports the successful construction of an unprecedented hybrid photocatalyst for the solar driven water splitting by covalently grafting a Ru phenanthroline PS onto **Fe@FeO$_x$** core/shell NPs through a phosphonate linker. Well controlled **Fe@FeO$_x$** core/shell NPs of *ca.* 11.5 ± 2.3 nm in diameter and with a γ Fe_2O_3 oxide shell of *ca.* 2.6 nm were synthesized. These NPs showed a better O_2 evolution electrocatalytic activity in alkaline conditions than in neutral ones, with an onset potential of 1.75 V and a Tafel slope value of 142 mV/decade at pH 13. Two synthetic pathways were investigated to graft the Ru PS at the surface of the **Fe@FeO$_x$ NPs**, *via* monophasic and biphasic processes in THF/H_2O or CH_2Cl_2/H_2O solvent mixtures, respectively. The monophasic process was found to be more efficient as it provided a higher grafting density at the surface of the NPs, 7 fold higher than that obtained by the biphasic process (56 and 9 Ru complexes per NP for the monophasic and biphasic processes, respectively). Finally, the efficient photocatalytic activity of the hybrid system prepared in monophasic conditions was demonstrated. The results obtained evidenced that the charge transfer between the grafted Ru PS and the **Fe@FeO$_x$** nanocatalyst was the bottleneck in the operation of these hybrid systems. At an applied potential of +1.0 V *versus* RHE and under a simulated 1 sun illumination, a catalytic rate of 0.02 O_2 Ru^{-1} s^{-1} was observed. Thus, increasing the grafting density of the Ru PS could be a way to improve the overall performance. Moreover, the covalent grafting was found to not only improve the photocatalytic activity (by *ca.* 9 fold compared with a system based on a simple physical adsorption) but also to significantly improve the stability of the photocatalyst. However, the charge recombination within the system remained important as evidenced by a rather high transient current. This may result from the quenching of the excited state of the Ru(II) complex by O_2 molecules accumulating on the surface of the **Fe@FeO$_x$** catalyst until a steady state in their evolution is reached. If so, a better evacuation of O_2 might improve the overall performance of the hybrid photocatalyst as well.

The covalent grafting of the hybrid *m* Fe@FeO$_x$**@Ru NPs** on the FTO electrode is now envisaged to avoid any possible leaching of the catalyst and to limit back electron transfer events happening during photocatalytic conditions.

4. EXPERIMENTAL SECTION

4.1. Materials. All chemicals used in the synthesis of the ligand and ruthenium(II) complex were purchased from commercial suppliers and used without further purification. 5 Bromo 1,10 phenanthroline[62−64] and *cis* $[Ru(phen)_2Cl_2]$[53,54] were synthesized as previously reported.

$[Fe[N(SiMe_3)_2]_2]_2$ was purchased from Nanomeps. Hexadecyl amine (HDA) (98%), oleic acid (99%), hydrogen chloride solution, 2 N in diethylether, trimethylamine *N* oxide (99%), *tert* butyl nitrite (90%), tetrabutylammonium hexafluorophosphate (98%), and Nafion (5 wt % in a mixture of lower aliphatic alcohols and water) were purchased from Sigma Aldrich and used without any purification. Hexadecylammonium chloride (HDA·HCl) was prepared as previously reported.[65] Mesitylene (99.7%) was purchased from Sigma Aldrich and distilled over sodium under an argon atmosphere. Octadecene (ODE) (90%) was purchased from Sigma Aldrich and dried over activated molecular sieve with a pore size of 0.4 nm under an argon atmosphere. Toluene, CH_2Cl_2, and diethyl ether were collected from an MBraun solvent purification system. Ethanol, absolute grade, was purchased from Sigma Aldrich and distilled over magnesium under an argon atmosphere. All the solvents were used after degassing by the freeze−pump−thaw technique. Milli Q water with conductivity at 28.2 Ω was used. FTO slides were cleaned by sonication for 30 min in acetone, 30 min in EtOH and then dried at room temperature for at least 1 h before use.

4.2. Synthesis of the $[Ru(phen)_2(phen\text{-}PO(OH)_2)]Cl_2$ Complex—[Ru−PO(OH)$_2$]Cl$_2$. *4.2.1. Synthesis of 5-P(O)(OH)$_2$-1,10-Phenanthroline (**phen-PO(OH)$_2$**).* Under an argon atmosphere, 200 mg of the already described 5 bromo 1,10 phenanthroline[63] (0.77 mmol) in toluene, 120 μL of commercially available $HP(O)(OEt)_2$ (0.93 mmol), 130 μL of triethylamine (0.93 mmol), 13 mg of $Pd(OAc)_2$ (0.058 mmol, 7%), and 65 mg of the ligand 1,1′ bis(diphenylphosphino)ferrocene (dppf) as the co catalyst (0.12 mmol) were stirred at reflux overnight. The starting brownish suspension turned to an orange solution. The solvent was evaporated to yield the crude material, which was purified by column chromatography on silica with a CH_2Cl_2/MeOH/NH_3·H_2O (96/2/2) mixture as an eluent. 55 mg of the desired compound (around 0.17 mmol, yield = 22%) was obtained, already partially deprotected and used as obtained.

4.2.2. Synthesis of $[Ru(phen)_2(phen\text{-}PO(OH)_2)](Cl)_2$. Under an argon atmosphere, 20 mg of the ligand **phen PO(OH)$_2$** (0.057 mmol) and 1 equiv of the precursor complex **[Ru(Phen)$_2$]Cl$_2$** (31.5 mg) were dissolved in 3 mL of degassed EtOH. The mixture was heated at reflux overnight. After evaporation of the solvent to dryness, 45 mg of an orange/red powder was obtained (yield = 10%). ^{1}H NMR (D_2O, 500 MHz): δ 9.04 (1H, d, *J* = 5 Hz), 8.48 (6H, d, *J* = 5 Hz), 8.10 (4H, s), 8.08−7.95 (6H, m), 7.58−7.45 ppm (6H, m); ^{31}P NMR (D_2O, 202 MHz): δ 7.13 ppm (P−OH, d, ^2J = 40 Hz); HRMS (ESI): *m*/*z* calcd for $RuC_{36}H_{24}N_6O_3PRu - H^+$, 721.0691 $[M - H^+]$; exp., 721.0698. Anal. Calcd for $[Ru(Phen)_2(PhenP(O)(OH)_2)]Cl_2 \cdot 7H_2O$ (M_w = 918.7 g/mol): C, 46.9; H, 3.8; and N, 9.2. Found: C, 47.1; H, 4.3; N, 9.2.

4.3. Synthesis of NPs. *4.3.1. Synthesis of Fe NPs.* Iron NPs were synthesized following a procedure reported by Gharbi *et al.*[48] with a minor modification. $[Fe[N(SiMe_3)_2]_2]_2$ (1.9 g, 2.5 mmol), HDA (2.4 g, 10 mmol), and HDA·HCl (2.1 g, 7.5 mmol) were dissolved in 100 mL mesitylene in a Fischer−Porter bottle in a glovebox. The dark brown solution was then immersed in an oil bath pre heated at 150 °C and kept at this temperature for 65 h. The reaction mixture was then cooled to room temperature and the mesitylene was removed by evaporation under reduced pressure. The iron NPs were dispersed in a solution of 8 mL oleic acid in 100 mL of toluene. The quantity of oleic acid was added in stoichiometric proportion *versus* the amine present in the crude mixture at the end of the reaction. Overnight, the NPs precipitated. The particles were then collected by magnetic separation and washed with toluene (4 × 50 mL), then with ethanol (3 × 50 mL) and afterward dried under vacuum. The NPs were kept inside a glovebox before use (recovered mass: 304 mg, ICP OES: Fe = 82 wt %).

*4.3.2. Synthesis of **Fe@FeO$_x$** NPs.* The iron oxide layer was achieved following the reported protocol[49] with minor modifications. In brief, 0.18 mmol of $(CH_3)_3NO$ (14 mg) were dispersed in 20 mL of ODE and flushed with argon for 30 min in a Fischer−Porter bottle. The mixture was heated up to 130 °C for 30 min. In another Fischer−Porter bottle, 160 mg of Fe NPs were dispersed in 4 mL of ODE and then this mixture was transferred to the $(CH_3)_3NO$ dispersion using a Teflon canula avoiding air exposure and heated for 2 h at 130 °C. Then, the mixture was heated up to 250 °C for 30 min, cooled to room temperature and opened in air. 25 mL of 1 propanol was added to this mixture and the black powder was collected using a magnet. The powder was washed with diethyl ether (1 × 30 mL) and then dried in air. (Recovered mass: 147 mg, ICP OES: Fe = 86.95 wt %).

*4.3.3. Synthesis of **Fe@FeO$_x$@Ru** Hybrid Nanomaterial **by the Biphasic Method**—b-Fe@FeO$_x$@Ru NPs.* 50 mg of **Fe@FeO$_x$ NPs** were added to 15 mL of CH_2Cl_2 in a closed glass tube and sonicated for 5 min. Then, 10 mL of a 2.96 × 10^{-4} M solution of **$[Ru(phen)_2(phen\ PO(OH)_2)]Cl_2 \cdot 7H_2O$** in Milli Q water was added. The mixture was mechanically stirred for 3 days till the aqueous phase became completely black, indicating that the transfer was efficient. The aqueous phase was then collected and purified by repeated magnetic precipitation−solvent removing−redispersion steps and washed with Milli Q water (5 × 30 mL), then with ethanol (1 × 30 mL) and diethyl ether (1 × 30 mL). The *b* **Fe@FeO$_x$@Ru NP** sample was dried in air before characterization. Recovered mass: 39.2 mg.

*4.3.4. Synthesis of **Fe@FeO$_x$@Ru** Hybrid Nanomaterial **by the Monophasic Method**—m-Fe@FeO$_x$@Ru NPs.* 21 mg of **Fe@FeO$_x$ NPs** were dispersed in 15 mL THF using sonication for 20 min. 10 mL of a 2.28 × 10^{-4} M solution of **$[Ru(phen)_2(phen\ PO(OH)_2)]Cl_2 \cdot 7H_2O$** in Milli Q water was added to this suspension. The reaction mixture was mechanically stirred at room temperature for 3 days. The *m* **Fe@FeO$_x$@Ru NP** sample was purified as described above for the biphasic method. Recovered mass: 17.5 mg.

4.4. Preparation of Photoanodes. Catalyst inks were prepared by sonicating 3 mg of each catalyst in 1 mL of a 1/4 (v/v) EtOH/H_2O solvent mixture together with 1 μL of Nafion 5 wt % as a linker.

m **Fe@FeO$_x$@Ru NP**, *b* **Fe@FeO$_x$@Ru NP**, and **Fe@FeO$_x$ NP** photoanodes were prepared by depositing 17 μL of the respective catalyst ink onto a FTO electrode (*S* = 0.283 cm^2, loading density of 1.8 × 10^{-4} g/cm^2) followed by a mild annealing process at 100 °C (a temperature at which the Ru complex is stable) in an oven for 5 h before testing their photocatalytic activity.

*4.4.1. Preparation of Non-bonded **Fe@FeO$_x$**//**Ru** Photoanode for Control Experiment.* A 1/4 (v/v) EtOH/H_2O solvent mixture together with 1 μL of Nafion 5 wt % was used to prepare a stock solution of $[Ru(phen)_3]Cl_2$ with concentration 3.8 × 10^{-5} M. A catalyst ink was prepared by the dispersion of **Fe@FeO$_x$ NPs** (3 mg) in 1 mL of this stock solution. Then, this ink was deposited onto a FTO electrode with a loading amount of 1.8 × 10^{-4} g/cm^2, followed by a mild annealing process at 100 °C for 5 h (a temperature at which the $[Ru(phen)_3]Cl_2$ complex is stable).

4.5. Photoelectrochemical Study. The photocatalytic activity was assayed in NaOH electrolyte solution, pH = 13. A conventional three electrode configuration was used with the photoanode (as prepared above) as a working electrode, Ag/AgCl/1 M KCl as a reference electrode, and a Pt wire as a counter electrode.

Light illumination was provided by a Xe arc lamp (LOT, Germany) with a 420 nm cutoff filter. The incident intensity was set to 100 mW/cm^2. Back side illumination was conducted, in which the incident light went through the transparent FTO electrode to the deposited catalyst on the photoanode. The potential polarization was conducted with a potential scan rate of 10 mV/s.

Potentials are quoted against the RHE using the following eq 1

$$E_{RHE} = E_{Ag/AgCl/KCl\ 3\ M} + 0.059 \times pH + E^0_{Ag/AgCl} \quad (1)$$

where the pH is 13 because the measurements were performed in 0.1 M NaOH, $E^0_{Ag/AgCl}$ is 0.21 V *versus* RHE.

The current density (*j*, mA/cm^2) was calculated by normalization to the geometric surface area of the FTO electrode (*S* = 0.283 cm^2).

4.6. Other Characterizations. The NP samples were characterized by different techniques in conventional (TEM) and high resolution (HR TEM) modes, atom resolved microscopy (ARM), WAXS, EXAFS, XPS, ICP OES, and Mössbauer spectroscopy.

4.6.1. TEM, HR-TEM, and ARM. These analyses were performed at the "Centre de Microcaractérisation Raymond Castaing" in Toulouse. The shape, size, and crystallinity of the NPs were examined in conventional TEM (JEOL, JEM 1011 microscope, operating at 100 kV, and a point resolution of 0.45 nm) and high resolution HAADF STEM (JEM, ARM200F microscope, operating at 200 kV, and a point resolution of 0.19 nm). TEM grids were prepared by casting a drop of the NP suspension onto a copper grid (400 hexagonal meshes, carbon coated). Then, the grids were further dried under vacuum for at least one night before introduction into the microscopy chamber. Size distributions were acquired by measuring a minimum of 250 objects using open source ImageJ software. Sizes are given as mean ± standard deviation according to a Gaussian fit of the corresponding size distribution. Fast Fourier transform analysis was carried out with Digital Micrograph software.

4.6.2. X-ray Photoelectron Spectroscopy. XPS measurements were performed at CIRIMAT ENSIACET in Toulouse on a Thermo Scientific K Alpha spectrometer equipped with a monochromatized Al Kα ($h\nu$ = 1486.6 eV) source. The X ray spot size was 400 μm. The pass energy was fixed at 30 eV with a step of 0.1 eV for core levels and 160 eV for surveys (step 1 eV). The spectrometer energy calibration was done using the Au $4f_{7/2}$ (83.9 ± 0.1 eV) and Ag $3d_{5/2}$ (368.2 ± 0.1 eV) photoelectron lines. XPS spectra were recorded in direct mode N (Ec) and the background signal was removed using the Shirley method. XPS high resolution spectra were recorded in order to extract the chemical environments of the studied species.

4.6.3. Inductively Coupled Plasma-Optical Emission Spectroscopy. Fe and Ru contents were determined by ICP OES using a PerkinElmer Optima 2100 DV instrument at LCC CNRS Toulouse. The samples were first digested into a mixture of HCl/HNO_3 (3:1 v/v) and then diluted with Milli Q water.

4.6.4. Wide-Angle X-ray Scattering. WAXS measurements were carried out at CEMES CNRS in Toulouse. The samples were sealed in 1.0 mm diameter Lindemann glass capillaries under an Ar atmosphere. The X ray scattering intensity measurements were performed using a dedicated two axis diffractometer equipped with a high energy resolution solid state detector allowing for the removal of the fluorescence from iron at the measurement step by electronic filtering, using the molybdenum Kα [0.071069 nm] radiation monochromatized by a flat graphite crystal. Time for data collection was typically 20 h for a set of 457 measurements collected at room temperature in the range $0° < \theta < 65°$ for equidistant s values [$s = 4\pi(\sin\theta/\lambda)$]. Radial distribution functions were obtained after Fourier transformation of the corrected and reduced data.

4.6.5. Extended X-ray Absorption Fine Structure. EXAFS spectra were recorded at the Fe K edge (7112 eV) at room temperature in a transmission mode on a BL8 beamline at Synchrotron Light Research Institute (SLRI, Nakhon Ratchasima, Thailand), using a Ge(220) double crystal monochromator. All data analysis was performed using ATHENA and ARTEMIS softwares.[66] Reference data from the pure γ Fe_2O_3 were imported from the Farrel Lytle database maintained by the International X ray Absorption Society.

4.6.6. Mössbauer Spectroscopy. The Mössbauer spectrum was obtained using a spectrometer running in the triangular symmetric mode for the velocity and a radioactive source of 1.85 GBq (50 mCi) Co^{57} diffused into a Rh matrix at LCC CNRS Toulouse. The temperature was regulated at 80 K in an Oxford cryostat. In the figures, dots represent the experimental data and continuous lines represent the curves corresponding to the four contributions used to fit the experimental data. The global fitting curve is also displayed as a solid line. Each contribution is defined by its isomer shift with respect to bcc iron (δ_o), quadrupolar splitting ($\Delta = \varepsilon_0$), and a distribution of hyperfine fields ($\mu_o H_{hyp}$). We have considered the same width (Γ) of the Lorentzian lines for all the contributions, Γ = 0.4 mm/s. The height ratios of line −1 to line −3 h_1/h_3 and line −2 to line −3 h_2/h_3 have been fixed for the elemental sextet to the theoretical values expected for randomly oriented systems, that is, $h_1/h_3 \approx 3$ and $h_2/h_3 \approx 2$.

■ ASSOCIATED CONTENT

● Supporting Information

The Supporting Information is available free of charge at https://pubs.acs.org/doi/10.1021/acsami.1c15051.

Synthesis and characterization of $[Ru{-}PO(OH)_2]Cl_2$ complex; complementary data on $Fe@FeO_x$ NPs and $Fe@FeO_x@Ru$ NPs; and complementary data on water oxidation catalysis (PDF)

■ AUTHOR INFORMATION

Corresponding Authors

Gilles Lemercier − *University of Reims Champagne Ardenne, ICMR, UMR CNRS, F 51687 Reims Cedex 2, France;* Email: gilles.lemercier@univ reims.fr

Phong D. Tran − *University of Science and Technology of Hanoi, Vietnam Academy of Science and Technology, 100000 Hanoi, Vietnam;* orcid.org/0000 0002 9561 6881; Email: tran dinh.phong@usth.edu.vn

Catherine Amiens − *CNRS, LCC (Laboratoire de Chimie de Coordination), F 31077 Toulouse Cedex 4, France; Université de Toulouse, UPS, INPT, F 31077 Toulouse Cedex 4, France;* Email: catherine.amiens@lcc toulouse.fr

Authors

Quyen T. Nguyen − *CNRS, LCC (Laboratoire de Chimie de Coordination), F 31077 Toulouse Cedex 4, France; Université de Toulouse, UPS, INPT, F 31077 Toulouse Cedex 4, France; University of Science and Technology of Hanoi, Vietnam Academy of Science and Technology, 100000 Hanoi, Vietnam*

Elodie Rousset − *University of Reims Champagne Ardenne, ICMR, UMR CNRS, F 51687 Reims Cedex 2, France*

Van T. H. Nguyen − *University of Science and Technology of Hanoi, Vietnam Academy of Science and Technology, 100000 Hanoi, Vietnam*

Vincent Colliere − *CNRS, LCC (Laboratoire de Chimie de Coordination), F 31077 Toulouse Cedex 4, France; Université de Toulouse, UPS, INPT, F 31077 Toulouse Cedex 4, France*

Pierre Lecante − *CEMES CNRS, Université de Toulouse, F 31055 Toulouse, France*

Wantana Klysubun − *Synchrotron Light Research Institute, 30000 Nakhon Ratchasima, Thailand*

Karine Philippot − *CNRS, LCC (Laboratoire de Chimie de Coordination), F 31077 Toulouse Cedex 4, France; Université de Toulouse, UPS, INPT, F 31077 Toulouse Cedex 4, France;* orcid.org/0000 0002 8965 825X

Jérôme Esvan − *CIRIMAT, Université de Toulouse, CNRS INPT UPS, 31030 Toulouse, France*

Marc Respaud − *Université de Toulouse, UPS, INPT, F 31077 Toulouse Cedex 4, France; LPCNO, INSA, 31077 Toulouse Cedex 4, France*

Complete contact information is available at: https://pubs.acs.org/10.1021/acsami.1c15051

Author Contributions

Conceptualization—P.D.T., G.L., and C.A.; data curation—E.R., P.L., J.E., V.C., and M.R.; formal analysis—Q.T.N.; funding acquisition—P.D.T., C.A., and K.P.; investigation—

E.R., Q.T.N., W.K., P.L., and V.T.H.N.; methodology—C.A. and P.D.T.; project administration—Q.T.N., C.A., and P.D.T.; supervision—P.D.T., G.L., E.R., C.A., and K.P.; validation—Q.T.N.; visualization—Q.T.N., E.R., M.R., J.E., and P.L.; writing—original draft—Q.T.N., C.A., E.R., P.L., and J.E.; writing—review and editing—Q.T.N., E.R., V.C., P.L., W.K., J.E., M.R., K.P., G.L., P.D.T., and C.A.

Notes

The authors declare no competing financial interest.

■ ACKNOWLEDGMENTS

We thank CNRS and Université de Toulouse Paul Sabatier for financial support. P.D.T. acknowledges the Vietnam Academy of Science and Technology for financial support through the grant ĐL0000.03/19 21. We thank the beamline BL8 team for setting up Fe K edge EXAFS experiment, the "Centre de Microcaractérisation Raymond Castaing" in Toulouse for access to the microscopes, JF Meunier for recording the Mössbauer spectrum, and Chuc T. Nguyen and Hoang V. Le for performing photoelectrochemical measurements. Q.T.N. acknowledges the French embassy in Hanoi for her PhD scholarship (Bourse d'Excellence 2018−2021).

■ REFERENCES

(1) Grimes, C. A.; Varghese, O. K.; Ranjan, S. Hydrogen Generation by Water Splitting. In *Light, Water, Hydrogen: The Solar Generation of Hydrogen by Water Photoelectrolysis*; Grimes, C. A., Varghese, O. K., Ranjan, S., Eds.; Springer US: Boston, MA, 2008; p 35.

(2) Liu, C.; Zhang, C.; Yin, G.; Zhang, T.; Wang, W.; Ou, G.; Jin, H.; Chen, Z. A Three Dimensional Branched TiO2 Photoanode with an Ultrathin Al2O3 Passivation Layer and a NiOOH Cocatalyst toward Photoelectrochemical Water Oxidation. *ACS Appl. Mater. Interfaces* **2021**, *13*, 13301−13310.

(3) Tayebi, M.; Lee, B. K. Recent Advances in BiVO4 Semi conductor Materials for Hydrogen Production using Photoelectro chemical Water Splitting. *Renewable Sustainable Energy Rev.* **2019**, *111*, 332−343.

(4) Yang, Q.; Du, J.; Li, J.; Wu, Y.; Zhou, Y.; Yang, Y.; Yang, D.; He, H. Thermodynamic and Kinetic Influence of Oxgen Vacancies on the Solar Water Oxidation Reaction of α Fe2O3 Photoanodes. *ACS Appl. Mater. Interfaces* **2020**, *12*, 11625−11634.

(5) Sherman, B. D.; Xie, Y.; Sheridan, M. V.; Wang, D.; Shaffer, D. W.; Meyer, T. J.; Concepcion, J. J. Light Driven Water Splitting by a Covalently Linked Ruthenium Based Chromophore Catalyst Assem bly. *ACS Energy Lett.* **2017**, *2*, 124−128.

(6) He, J.; Wang, B.; Chang, S.; Chen, T. Ruthenium Based Photosensitizers for Dye Sensitized Solar Cells. In *Organometallics and Related Molecules for Energy Conversion*; Wong, W. Y., Ed.; Springer Berlin Heidelberg: Berlin, Heidelberg, 2015; pp 91−114.

(7) Kirner, J. T.; Stracke, J. J.; Gregg, B. A.; Finke, R. G. Visible Light Assisted Photoelectrochemical Water Oxidation by Thin Films of a Phosphonate Functionalized Perylene Diimide Plus CoOx Cocatalyst. *ACS Appl. Mater. Interfaces* **2014**, *6*, 13367−13377.

(8) Kirner, J. T.; Finke, R. G. Sensitization of Nanocrystalline Metal Oxides with a Phosphonate Functionalized Perylene Diimide for Photoelectrochemical Water Oxidation with a CoOx Catalyst. *ACS Appl. Mater. Interfaces* **2017**, *9*, 27625−27637.

(9) Wang, L.; Bledowski, M.; Ramakrishnan, A.; König, D.; Ludwig, A.; Beranek, R. Dynamics of Photogenerated Holes in TiO2 polyheptazine Hybrid Photoanodes for Visible Light Driven Water Splitting. *J. Electrochem. Soc.* **2012**, *159*, H616−H622.

(10) Wang, L.; Mitoraj, D.; Turner, S.; Khavryuchenko, O. V.; Jacob, T.; Hocking, R. K.; Beranek, R. Ultrasmall CoO(OH)x Nanoparticles as a Highly Efficient "True" Cocatalyst in Porous Photoanodes for Water Splitting. *ACS Catal.* **2017**, *7*, 4759−4767.

(11) Swierk, J. R.; Méndez Hernández, D. D.; McCool, N. S.; Liddell, P.; Terazono, Y.; Pahk, I.; Tomlin, J. J.; Oster, N. V.; Moore, T. A.; Moore, A. L.; Gust, D.; Mallouk, T. E. Metal free Organic Sensitizers for Use in Water Splitting Dye Sensitized Photoelectro chemical Cells. *Proc. Natl. Acad. Sci. U.S.A.* **2015**, *112*, 1681−1686.

(12) Bornoz, P.; Prévot, M. S.; Yu, X.; Guijarro, N.; Sivula, K. Direct Light Driven Water Oxidation by a Ladder Type Conjugated Polymer Photoanode. *J. Am. Chem. Soc.* **2015**, *137*, 15338−15341.

(13) Guan, J.; Li, D.; Si, R.; Miao, S.; Zhang, F.; Li, C. Synthesis and Demonstration of Subnanometric Iridium Oxide as Highly Efficient and Robust Water Oxidation Catalyst. *ACS Catal.* **2017**, *7*, 5983−5986.

(14) Jiang, B.; Kim, J.; Guo, Y.; Wu, K. C. W.; Alshehri, S. M.; Ahamad, T.; Alhokbany, N.; Henzie, J.; Yamachi, Y. Efficient Oxygen Evolution on Mesoporous IrOx Nanosheets. *Catal. Sci. Technol.* **2019**, *9*, 3697−3702.

(15) Deng, X.; Tüysüz, H. Cobalt Oxide Based Materials as Water Oxidation Catalyst: Recent Progress and Challenges. *ACS Catal.* **2014**, *4*, 3701−3714.

(16) Gujral, S. S.; Simonov, A. N.; Higashi, M.; Fang, X. Y.; Abe, R.; Spiccia, L. Highly Dispersed Cobalt Oxide on TaON as Efficient Photoanodes for Long term Solar Water Splitting. *ACS Catal.* **2016**, *6*, 3404−3417.

(17) Kanan, M. W.; Nocera, D. G. In Situ Formation of an Oxygen Evolving Catalyst in Neutral Water Containing Phosphate and Co2+. *Science* **2008**, *321*, 1072−1075.

(18) Kanan, M. W.; Yano, J.; Surendranath, Y.; Dincă, M.; Yachandra, V. K.; Nocera, D. G. Structure and Valency of a Cobalt Phosphate Water Oxidation Catalyst Determined by In Situ X ray Spectroscopy. *J. Am. Chem. Soc.* **2010**, *132*, 13692−13701.

(19) Zhong, D. K.; Cornuz, M.; Sivula, K.; Grätzel, M.; Gamelin, D. R. Photo assisted Electrodeposition of Cobalt Phosphate (Co Pi) Catalyst on Hematite Photoanodes for Solar Water Oxidation. *Energy Environ. Sci.* **2011**, *4*, 1759−1764.

(20) Chemelewski, W. D.; Lee, H. C.; Lin, J. F.; Bard, A. J.; Mullins, C. B. Amorphous FeOOH Oxygen Evolution Reaction Catalyst for Photoelectrochemical Water Splitting. *J. Am. Chem. Soc.* **2014**, *136*, 2843−2850.

(21) Feng, J. X.; Xu, H.; Dong, Y. T.; Ye, S. H.; Tong, Y. X.; Li, G. R. FeOOH/Co/FeOOH Hybrid Nanotube Arrays as High Perform ance Electrocatalysts for the Oxygen Evolution Reaction. *Angew. Chem., Int. Ed.* **2016**, *55*, 3694−3698.

(22) Hu, J.; Li, S.; Chu, J.; Niu, S.; Wang, J.; Du, Y.; Li, Z.; Han, X.; Xu, P. Understanding the Phase Induced Electrocatalytic Oxygen Evolution Reaction Activity on FeOOH Nanostructures. *ACS Catal.* **2019**, *9*, 10705−10711.

(23) Mukai, K.; Suzuki, T. M.; Uyama, T.; Nonaka, T.; Morikawa, T.; Yamada, I. High Pressure Synthesis of ε FeOOH from β FeOOH and Its Application to the Water Oxidation Catalyst. *RSC Adv.* **2020**, *10*, 44756−44767.

(24) Matheu, R.; Garrido Barros, P.; Gil Sepulcre, M.; Ertem, M. Z.; Sala, X.; Gimbert Suriñach, C.; Llobet, A. The Development of Molecular Water Oxidation Catalysts. *Nat. Rev. Chem.* **2019**, *3*, 331−341.

(25) Blakemore, J. D.; Crabtree, R. H.; Brudvig, G. W. Molecular Catalysts for Water Oxidation. *Chem. Rev.* **2015**, *115*, 12974−13005.

(26) Kirner, J. T.; Finke, R. G. Water Oxidation Photoanodes Using Organic Light Harvesting Materials: A Review. *J. Mater. Chem. A* **2017**, *5*, 19560−19592.

(27) Yu, Z.; Li, F.; Sun, L. Recent Advances in Dye Sensitized Photoelectrochemical Cells for Solar Hydrogen Production Based on Molecular Components. *Energy Environ. Sci.* **2015**, *8*, 760−775.

(28) Chen, X.; Ren, X.; Liu, Z.; Zhuang, L.; Lu, J. Promoting the Photoanode Efficiency for Water Splitting by Combining Hematite and Molecular Ru Catalysts. *Electrochem. Commun.* **2013**, *27*, 148−151.

(29) Kim, T. W.; Choi, K. S. Nanoporous BiVO4 Photoanodes with Dual Layer Oxygen Evolution Catalysts for Solar Water Splitting. *Science* **2014**, *343*, 990−994.

(30) Nellist, M. R.; Qiu, J.; Laskowski, F. A. L.; Toma, F. M.; Boettcher, S. W. Potential Sensing Electrochemical AFM Shows CoPi as a Hole Collector and Oxygen Evolution Catalyst on BiVO4 Water Splitting Photoanodes. *ACS Energy Lett.* **2018**, *3*, 2286−2291.
(31) Lichterman, M. F.; Shaner, M. R.; Handler, S. G.; Brunschwig, B. S.; Gray, H. B.; Lewis, N. S.; Spurgeon, J. M. Enhanced Stability and Activity for Water Oxidation in Alkaline Media with Bismuth Vanadate Photoelectrodes Modified with a Cobalt Oxide Catalytic Layer Produced by Atomic Layer Deposition. *J. Phys. Chem. Lett.* **2013**, *4*, 4188−4191.
(32) Youngblood, W. J.; Lee, S. H. A.; Kobayashi, Y.; Hernandez Pagan, E. A.; Hoertz, P. G.; Moore, T. A.; Moore, A. L.; Gust, D.; Mallouk, T. E. Photoassisted Overall Water Splitting in a Visible Light Absorbing Dye Sensitized Photoelectrochemical Cell. *J. Am. Chem. Soc.* **2009**, *131*, 926−927.
(33) Lee, S. H. A.; Zhao, Y.; Hernandez Pagan, E. A.; Blasdel, L.; Youngblood, W. J.; Mallouk, T. E. Electron Transfer Kinetics in Water Splitting Dye Sensitized Solar Cells Based on Core Shell Oxide Electrodes. *Faraday Discuss.* **2012**, *155*, 165−176.
(34) De Tovar, J.; Romero, N.; Denisov, S. A.; Bofill, R.; Gimbert Suriñach, C.; Ciuculescu Pradines, D.; Drouet, S.; Llobet, A.; Lecante, P.; Colliere, V.; Freixa, Z.; McClenaghan, N.; Amiens, C.; García Antón, J.; Philippot, K.; Sala, X. Light Driven Water Oxidation using Hybrid Photosensitizer Decorated Co3O4 Nanoparticles. *Mater. Today Energy* **2018**, *9*, 506−515.
(35) Jung, S.; McCrory, C. C. L.; Ferrer, I. M.; Peters, J. C.; Jaramillo, T. F. Benchmarking Nanoparticulate Metal Oxide Electro catalysts for the Alkaline Water Oxidation Reaction. *J. Mater. Chem. A* **2016**, *4*, 3068−3076.
(36) Kwong, W. L.; Lee, C. C.; Shchukarev, A.; Björn, E.; Messinger, J. High Performance Iron (III) Oxide Electrocatalyst for Water Oxidation in Strong Acidic Media. *J. Catal.* **2018**, *365*, 29−35.
(37) Hagfeldt, A.; Grätzel, M. Molecular Photovoltaics. *Acc. Chem. Res.* **2000**, *33*, 269−277.
(38) Kuang, D.; Ito, S.; Wenger, B.; Klein, C.; Moser, J. E.; Humphry Baker, R.; Zakeeruddin, S. M.; Grätzel, M. High Molar Extinction Coefficient Heteroleptic Ruthenium Complexes for Thin Film Dye Sensitized Solar Cells. *J. Am. Chem. Soc.* **2006**, *128*, 4146−4154.
(39) Balzani, V.; Clemente León, M.; Credi, A.; Ferrer, B.; Venturi, M.; Flood, A. H.; Stoddart, J. F. Autonomous Artificial Nanomotor Powered by Sunlight. *Proc. Natl. Acad. Sci. U.S.A.* **2006**, *103*, 1178−1183.
(40) Heinemann, F.; Karges, J.; Gasser, G. Critical Overview of the Use of Ru(II) Polypyridyl Complexes as Photosensitizers in One Photon and Two Photon Photodynamic Therapy. *Acc. Chem. Res.* **2017**, *50*, 2727−2736.
(41) Stephenson, M.; Reichardt, C.; Pinto, M.; Wächtler, M.; Sainuddin, T.; Shi, G.; Yin, H.; Monro, S.; Sampson, E.; Dietzek, B.; McFarland, S. A. Ru(II) Dyads Derived from 2 (1 Pyrenyl) 1H Imidazo[4,5 f][1,10]phenanthroline: Versatile Photosensitizers for Photodynamic Applications. *J. Phys. Chem. A* **2014**, *118*, 10507−10521.
(42) Girardot, C.; Cao, B.; Mulatier, J. C.; Baldeck, P. L.; Chauvin, J.; Riehl, D.; Delaire, J. A.; Andraud, C.; Lemercier, G. Ruthenium (II) Complexes for Two Photon Absorption Based Optical Power Limiting. *ChemPhysChem* **2008**, *9*, 1531−1535.
(43) Four, M.; Riehl, D.; Mongin, O.; Blanchard Desce, M.; Lawson Daku, L. M.; Moreau, J.; Chauvin, J.; Delaire, J. A.; Lemercier, G. A Novel Ruthenim (II) Complex for Two Photon Absorption Based Optical Power Limiting in the Near IR Range. *Phys. Chem. Chem. Phys.* **2011**, *13*, 17304−17312.
(44) Parikh, S. J.; Chorover, J. ATR FTIR Spectroscopy Reveals Bond Formation During Bacterial Adhesion to Iron Oxide. *Langmuir* **2006**, *22*, 8492−8500.
(45) Basly, B.; Popa, G.; Fleutot, S.; Pichon, B. P.; Garofalo, A.; Ghobril, C.; Billotey, C.; Berniard, A.; Bonazza, P.; Martinez, H.; Felder Flesch, D.; Begin Colin, S. Effect of the Nanoparticle Synthesis Method on Dendronized Iron Oxides as MRI Contrast Agents. *Dalton Trans.* **2013**, *42*, 2146−2157.
(46) Mohapatra, S.; Pramanik, P. Synthesis and Stability of Functionalized Iron Oxide Nanoparticles Using Organophosphorus Coupling Agents. *Colloids Surf., A* **2009**, *339*, 35−42.
(47) Daou, T. J.; Begin Colin, S.; Grenèche, J. M.; Thomas, F.; Derory, A.; Bernhardt, P.; Legaré, P.; Pourroy, G. Phosphate Adsorption Properties of Magnetite Based Nanoparticles. *Chem. Mater.* **2007**, *19*, 4494−4505.
(48) Gharbi, K.; Salles, F.; Mathieu, P.; Amiens, C.; Collière, V.; Coppel, Y.; Philippot, K.; Fontaine, L.; Montembault, V.; Smiri, L. S.; Ciuculescu Pradines, D. Alkyl Phosphonic Acid Based Ligands as Tools for Converting Hydrophobic Iron Nanoparticles into Water Soluble Iron Iron Oxide Core Shell Nanoparticles. *New J. Chem.* **2017**, *41*, 11898−11905.
(49) Peng, S.; Wang, C.; Xie, J.; Sun, S. Synthesis and Stabilization of Monodisperse Fe Nanoparticles. *J. Am. Chem. Soc.* **2006**, *128*, 10676−10677.
(50) Mathieu, P.; Coppel, Y.; Respaud, M.; Nguyen, Q. T.; Boutry, S.; Laurent, S.; Stanicki, D.; Henoumont, C.; Novio, F.; Lorenzo, J.; Montpeyó, D.; Amiens, C. Silica Coated Iron/Iron Oxide Nano particles as a Nano Platform for T2 Weighted Magnetic Resonance Imaging. *Molecules* **2019**, *24*, 4629.
(51) Da Costa, G. M.; De Grave, E.; Vandenberghe, R. E. Mossbauer Studies of Magnetite and Al substituted Maghemites. *Hyperfine Interact.* **1998**, *117*, 207−243.
(52) Mitrofanov, A.; Lemeune, A. B.; Stern, C.; Guilard, R.; Gulyukina, N.; Beletskaya, I. Palladium Catalyzed Synthesis of Mono and Diphosphorylate 1,10 Phenanthrolines. *Synthesis* **2012**, *44*, 3805−3810.
(53) Giordano, P. J.; Bock, C. R.; Wrighton, M. S. Excited State Proton Transfer of Ruthenium (II) Complexes of 4,7 dihydroxy 1,10 phenanthroline. Increased Acidity in the Excited State. *J. Am. Chem. Soc.* **1978**, *100*, 6960−6965.
(54) Hackett, J. W.; Turro, C. Luminescent $Ru(phen)_n(bps)_{3-n}^{2n-4}$ Complexes (n=0 3) as Probes of Electrostatic and Hydrophobic Interactions with Micellar Media. *Inorg. Chem.* **1998**, *37*, 2039−2046.
(55) It is worth noting that NH_4Cl was no longer detected, suggesting its complete removal during the grafting process (Supporting Information, Figure S18).
(56) Agnès, C.; Arnault, J. C.; Omnès, F.; Jousselme, B.; Billon, M.; Bidan, G.; Mailley, P. XPS Study of Ruthenium Tris Bipyridine Electrografted from Diazonium Salt Derivative on MicroCrystalline Boron Doped Diamond. *Phys. Chem. Chem. Phys.* **2009**, *11*, 11647−11654.
(57) Touihri, S.; Safoula, G.; Bernéde, J. C. Properties of Chlorine Doped Poly(N vinylcarbazole) Thin Films. *Polym. Degrad. Stab.* **1998**, *60*, 481−485.
(58) Youngblood, W. J.; Lee, S. H. A.; Maeda, K.; Mallouk, T. E. Visible Light Water Splitting Using Dye Sensitized Oxide Semi conductors. *Acc. Chem. Res.* **2009**, *42*, 1966−1973.
(59) Le Formal, F.; Sivula, K.; Grätzel, M. The Transient Photocurrent and Photovoltage Behavior of a Hematite Photoanode under Working Conditions and the Influence of Surface Treatments. *J. Phys. Chem. C* **2012**, *116*, 26707−26720.
(60) Hu, L.; Liu, X.; Dalgleish, S.; Matsushita, M. M.; Yoshikawa, H.; Awaga, K. Organic Optoelectronic Interfaces with Anomalous Transient Photocurrent. *J. Mater. Chem. C* **2015**, *3*, 5122−5135.
(61) Lemercier, G.; Bonne, A.; Four, M.; Lawson Daku, L. M. 3MLCT Excited States in Ru(II) Complexes: Reactivity and Related Two Photon Absorption Applications in the Near Infrared Spectral Range. *C. R. Chim.* **2008**, *11*, 709−715.
(62) Hissler, M.; Connick, W. B.; Geiger, D. K.; McGarrah, J. E.; Lipa, D.; Lachicotte, R. J.; Eisenberg, R. Platinum Diimine Bis(acetylide) Complexes: Synthesis, Characterization, and Lumines cence Properties. *Inorg. Chem.* **2000**, *39*, 447−457.
(63) Girardot, C.; Lemercier, G.; Mulatier, J. C.; Chauvin, J.; Baldeck, P. L.; Andraud, C. Novel Ruthenium (II) and Zinc (II)

Complexes for Two Photon Absorption Related Applications. *Dalton Trans.* **2007**, 3421−3426.
(64) Girardot, C.; Lemercier, G.; Mulatier, J. C.; Andraud, C.; Chauvin, J.; Baldeck, P. L. Novel 5 (Oligofluorenyl) 1,10 Phenanthro line Type Ligands: Synthesis, Linear and Two photon Absorption Properties. *Tetrahedron Lett.* **2008**, *49*, 1753−1758.
(65) Meffre, A.; Lachaize, S.; Gatel, C.; Respaud, M.; Chaudret, B. Use of Long Chain Amine as a Reducing Agent for the Synthesis of High Quality Monodisperse Iron(0) Nanoparticles. *J. Mater. Chem.* **2011**, *21*, 13464−13469.
(66) Ravel, B.; Newville, M. Athena, Artemis, Hephaestus: Data Analysis for X ray Absorption Spectroscopy Using IFEFFIT. *J. Synchrotron Radiat.* **2005**, *12*, 537−541.